Available online at www.sciencedirect.com
ScienceDirect
Comput. Methods Appl. Mech. Engrg. 401 (2022) 115635
Computer methods in applied mechanics and engineering
www.elsevier.com/locate/cma

# Bone remodelling-based numerical evaluation of personalized masticatory forces from CT-scans

J. Gutiérrez-Gil[a,*], E. Nadal[a], K. Bouza[b], M. Tur[a], C.M. Atienza[a], O. Allix[c], J.J. Ródenas[a]

[a] *Instituto Universitario de Ingeniería Mecánica y Biomecánica, Universitat Politècnica de València, Spain*
[b] *Departamento de Ciencias de la Salud - Odontología, Universidad Europea de Valencia, Spain*
[c] *ENS Paris-Saclay, LMPS - Laboratoire de Mécanique Paris-Saclay, CentraleSupélec, Université Paris-Saclay, CNRS - Centre national de la recherche scientifique, France*

Received 10 June 2022; received in revised form 22 July 2022; accepted 2 September 2022
Available online 3 October 2022

**Abstract**

In recent years, the patient specific medical scenario has gained increasing popularity in health and engineering research. Unlike the standard medical paradigm (generalized treatment), personalized health techniques are oriented towards suiting the specific demands of a given patient, resulting in solutions that increase the success of the medical procedure. The idea of computer oriented, or *in silico*, medical experimentation has proven to be an effective tool to permit the implementation of patient specific medicine.

Bone remodelling (BR) simulation intends to predict bone distribution changes due to the specific living conditions of a certain bone under the patient's loading conditions. Unfortunately, it is usually difficult to obtain the simulation conditions affecting this process which are particular in each case. In this sense, the objective of this work is to present a procedure to adjust the patient-dependent biomechanical factors affecting bone growth and ingrowth, in order to reduce the computational uncertainty of the BR simulation. Assuming that the medical image represents a bone distribution in remodelling homeostasis, the optimization of parameters is driven by the search of a stationary remodelling state of the bone. The methodology is tested in a synthetic problem and also applied in the context of a human mandible in which mastication forces are obtained.


*Keywords:* Bone remodelling; cgFEM; Parameter search; Model adaptation; Patient specific

## 1. Introduction

Approaching the problem of personalized medical simulation in an *in silico* manner unleashes a large potential for the improvement of short and long-term quality of live of patients. This allows non-invasive, inexpensive and fast simulations, and therefore permits guided testing where many design variations or even medical protocols can be tested and adapted to a specific patient. One of the greatest limitations in this paradigm is the accurate modelling of the specific simulation conditions, specially those which are very dependent on the biology and lifestyle of each

* Corresponding author.
*E-mail addresses:* jorgugi1@upv.es (J. Gutiérrez-Gil), ennaso@upvnet.upv.es (E. Nadal), kheira.bouza@uem.es (K. Bouza), manuel.tur@mcm.upv.es (M. Tur), carlos.atienza@ibv.org (C.M. Atienza), olivier.allix@ens-paris-saclay.fr (O. Allix), jjrodena@mcm.upv.es (J.J. Ródenas).

https://doi.org/10.1016/j.cma.2022.115635

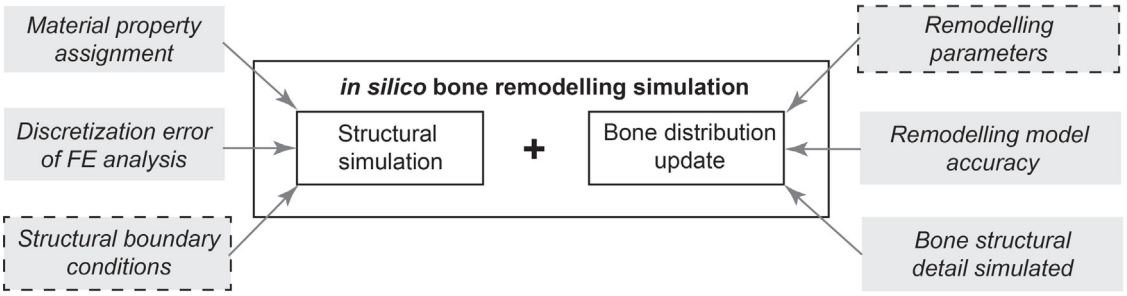


**Fig. 1.** Main sources of uncertainties affecting the two main parts of a bone remodelling simulation: structural simulations to obtain a remodelling stimulus, and a bone distribution update scheme to adequate the bone density correspondingly. This work focuses on a procedure to obtain some Structural boundary conditions and/or Remodelling parameters which mimic those specific from a given case, thus reducing important sources of modelling errors.

subject. Typical sources of modelling uncertainties affecting personalized bone remodelling simulations are shown in Fig. 1. This work proposes a methodology to reduce some of them.

Bone adaptation is a dynamic process where the bone structure responds to the ongoing mechanical stimuli [1,2]. Although the stimuli could be considered stationary in an adult bone, there are some situations where it can be abruptly modified, leading to the adaptive response of the bone. These cases require the accurate bone remodelling prediction in order to design tailor-made medical solutions.

An example is prostheses implantation where, in most cases, bone architectural redistribution is a response to the sudden, non physiological change in structural stimuli that can lead to implant failure. This is typically caused by the so-called Stress Shielding phenomenon, which leads to bone 'laziness' and can end in implant failure [3]. Consequently, prosthetic design considering short and long term bone adaptation has been an active research field in recent times [4].

The simulation of the bone remodelling process usually considers a Finite Element Method (FEM) analysis to compute the mechanical stimuli in a certain simulation period. Its outputs are the bone stress and strain data, which are then translated into a bone distribution update given a certain bone remodelling strategy, since this process in mainly mechanically guided [5]. When solving this *in silico* problem, there are many sources of uncertainties (shown in Fig. 1), which ultimately reduce the accuracy of bone density prediction and so the fitness of the medical protocol selection. This work will focus on adjusting Structural boundary conditions, while future works will explore adjusting also Remodelling parameters.

In the existent literature related to applied bone remodelling simulation [6,7], patient-specific data is usually not considered in the configuration of structural loads (diversity, positioning, orientation, amplitude) nor the remodelling parameters definition. This is specially relevant when studying bone structures affected by complex loading scenarios and wide subject variability, like for example, in the human jaw and its masticatory cycle. In such case, some authors [8,9], consider complex biomechanical models to obtain the loads at teeth, but even these require some generic assumptions in the masticatory cycle and/or patient specific biological parameters which are difficult to measure (such as muscle activation). Moreover, other biological parameters included in the remodelling algorithms are not usually adapted to the specific patient. They, however, can affect in a relevant manner the short and long-term bone distribution outcome, specially in phenomenological remodelling models with a few but important parameters [6,8,10].

The present work aims at using easily available patient specific information to evaluate subject dependent conditions affecting bone structural simulation towards an improved accuracy of the bone adaptation model. First, we consider an initial medical image which represents an assumable bone remodelling stationary state, then a finite element model is generated from this image through the Cartesian grid FEM (cgFEM) technology, explained in the next section. Using this model and some candidate personalized simulation parameters selected by an optimization algorithm, a null-remodelling situation is searched. This scenario has equivalent conditions to those patient-specific, which lead to the medical image.

The problem of load prediction from bone morphology has been explored recently. For example, the authors in [11] scaled the loading conditions to maximize the uniformity of the loading field in a test micro-CT scan. Then,

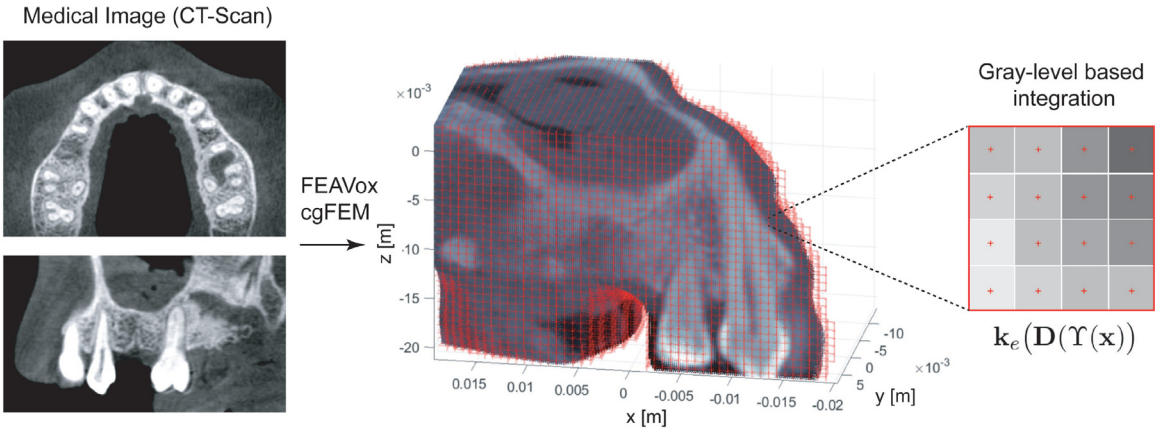


**Fig. 2.** FEM models from medical images are obtained through cgFEM, where the element stiffness matrix $\mathbf{k}_e$ is computed using a material matrix $\mathbf{D}(\Upsilon(\mathbf{x}))$ which is spatially dependent with the medical image Hounsfield value $\Upsilon$ [14].

later in [12], they applied the method in a non clinical micro-CT scan of a human forearm. Other approaches [13] include solving the inverse problem using neural-network trained models, which also considered the issue of non uniqueness of the density distribution. Until the best of the authors' knowledge, a framework to predict model parameters through the search of a homeostatic stimulus state, based on 3D images obtained in the standard medical practice, has not been studied yet.

After this introduction, the methodological foundations are described in Section 2. In Section 3 we focus on the parameter fitting procedure itself, followed by the exposition and analysis of numerical results in Section 4, both through a synthetic model example and a case study using a real medical image.

## 2. Methodology

In this section, the existing technologies, procedures and theoretical background used in the work are summarized. First, the generation cgFEM models using medical images is briefly seen, followed by a description of the remodelling algorithm and its integration in the cgFEM framework.

### *2.1. Medical image-based cgFEM*

Normally, when creating bone-implant FE models from medical images, for example from three dimensional CT Scans, there is a laborious segmentation processing of the medical image so that the FEM model is finally created. By applying the cgFEM through the software FEAVox [14], the creation of FE models from medical images is made straightforwardly. Fig. 2 illustrates the main stages of the process, where a cgFEM mesh is generated from a coarsely segmented bone domain merely to reduce the amount of voxels to be considered in the FE model.

Due to the Cartesian mesh structure of the cgFEM, compatible with 3D images, it is possible to directly identify a number of voxels into each finite element. The element stiffness matrix $\mathbf{k}_e$ is integrated using the information of the voxels contained in it, each voxel with an associated material property derived from the image intensity values. Though there are various integration techniques which can be adopted, the so called Riemann sum method is adopted in this work. Here, we consider a spatially dependent material property matrix $\mathbf{D}(\Upsilon(\mathbf{x}))$ in the calculation of the element stiffness $\mathbf{k_e}$ matrix from the contribution of each integration point $i_p$ [14], as:

$$\mathbf{k_e} = \sum_{i_p=1}^{n_{i_p}} \mathbf{B^T}(\xi_j)\mathbf{D}(\xi_j)\mathbf{B}(\xi_j)|\mathbf{J}(\xi_\mathbf{j})|w_j \tag{1}$$

$n_{i_p}$ being the number of element integration points (in this work being one per voxel located at its centre), $\mathbf{B^T}$ a matrix containing the derivative of the shape functions, $|\mathbf{J}|$ the Jacobian matrix determinant, and $w_j$ the weight associated to each integration point. As it can be seen, the material properties of the image are first momentum

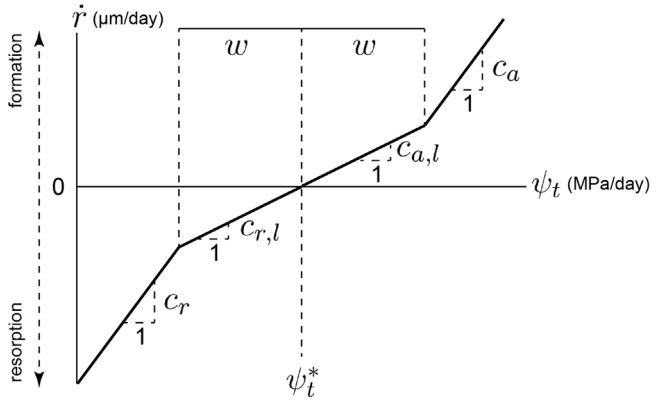


**Fig. 3.** Remodelling law.

averaged at element level, thus the anisotropic bone structure distribution can taken into account. The Hounsfield level of the image can be related with different material properties (for example, the Young modulus), using the available literature data [6,10,14].

Taking this integration procedure for the stiffness matrix into account, the linear elasticity problem is defined as follows:

$$\begin{aligned} &\text{Find } \mathbf{u} \in V : \forall \mathbf{v} \in V \\ &a(\mathbf{u}, \mathbf{v}) = l(\mathbf{v}) \qquad \text{where} \\ &a(\mathbf{u}, \mathbf{v}) = \int_{\Omega} \boldsymbol{\varepsilon}(\mathbf{u})^T \boldsymbol{\sigma}(\mathbf{v}) \, \mathrm{d}\Omega \\ &l(\mathbf{v}) = \int_{\Omega} \mathbf{b}^T \mathbf{v} \, \mathrm{d}\Omega + \int_{\Gamma_N} \mathbf{t}^T \mathbf{v} \, \mathrm{d}\Gamma, \end{aligned} \tag{2}$$

where the displacement field is defined as $\mathbf{u}$, the strain field as $\boldsymbol{\varepsilon}$, the stress field is denoted as $\boldsymbol{\sigma}$, and boundary denoted by $\partial\Omega$. Prescribed tractions denoted by $\mathbf{t}$ are imposed over the part $\Gamma_N$ of the boundary, while displacements denoted by $\bar{\mathbf{u}}$ are prescribed over the complementary part $\Gamma_D$ of the boundary. Body loads are denoted as $\mathbf{b}$. It is highlighted that in this work, body loads are considered to be zero since the weight of the bodies is not significant compared to the masticatory forces. Problem (2) is solved in the space $V = \{\mathbf{v} \mid \mathbf{v} \in \left[H^1(\Omega)\right]^d\}$ being $d$ the dimension of the problem. It can be observed that problem (2) is not solvable since Dirichlet boundary conditions are not considered. cgFEM imposes the essential boundary conditions, $\bar{\mathbf{u}}$, via Lagrange multipliers [15]. The choice of the Lagrange multipliers space is critical and not evident in some situations, therefore in the cgFEM context a stabilization technique, also presented in [15], is used. Additionally, the solution space also has to be stabilized because $\partial\Omega$ can arbitrarily cut the elements, leading to ill-conditioning issues [16]. The continuous problem is solved by using a discretization with linear elements.

### 2.2. Bone remodelling simulation

The remodelling model considered is the model presented in [17], and applied in recent works, either in the isotropic version [10] or with anisotropic enhanced formulations [6,18]. For the sake of simplicity, remodelling isotropy is considered in the present paper.

The phenomenological remodelling model used is inspired by biological homeostatic adaptation of bone. It is formulated in terms of daily bone adaptation towards the amount of mechanical stimulation which is "adequate" for a given bone at a given tissue point, also called reference stimulus $\psi_t^*$.

This adaptation process is driven by a certain remodelling law, such as the one illustrated in Fig. 3.

Here, either formation, resorption or bone maintenance rates $\dot{r}$ depend on the relationship between the actual bone stimulus at tissue level $\psi_t$ and $\psi_t^*$. $w$ is the half width of the so called 'lazy zone', which determines the threshold inside which the actual stimulus degree $\psi_t$ is not sufficiently different from $\psi_t^*$ to generate a maximum

variation. Outside the lazy zone, the rate of response formation and resorption is determined by parameters $c_a$ and $c_r$, respectively. Inside the lazy zone, formation and resorption rates are determined by $c_{a,l}$ and $c_{r,l}$, respectively, these being typically lower than $c_a$ and $c_r$, given the proximity to the homeostatic point were $\psi_t = \psi_t^*$. When $w$ describes the range of no density variation $\dot{r} = 0$, this range is described as a 'dead zone', however, since the existence of an actual tissue stimulus range where no remodelling occurs is still unclear [19], in this work $w$ is considered to be zero. This also favours the uniqueness of the long-term density solution [19], which is desired when applying the fitting procedure described in this work. Finally, as an additional approximation, this work also considers $c = c_a = c_r = c_{a,l} = c_{r,l}$.

$\psi_t$ at the tissue level, is derived through:

$$\psi_t = \left(\frac{\hat{\rho}}{\rho}\right)^2 \psi \ , \tag{3}$$

where $\rho$ and $\hat{\rho}$ are the apparent and cortical density of bone ($\hat{\rho} = 2.1$ g/cm$^3$), respectively. $\psi$ is the computed stimulus at the continuum level by load case $i$, obtained as:

$$\psi = n^{1/m}\hat{\sigma}. \tag{4}$$

Here, $n$ is the number of load cycles of the particular load condition being simulated and $m$ is a constant [8]. As seen later, $n$ is taken to be constant for the different problems studied. $\hat{\sigma}$ is the so called effective stress value obtained from the FEM, defined as:

$$\hat{\sigma} = \sqrt{2EU}, \tag{5}$$

$$E = 3388\rho^{2.58}, \tag{6}$$

$E$ being the Young's modulus expressed in MPa, and obtained through Eq. (6), a relationship given by [20] and used in [8], with $\rho$ expressed in g/cm$^3$. $U$ corresponds to the strain energy density at a particular tissue point for a given loading situation.

Given that $\psi$ (and therefore $\psi_t$) is related to the strain energy density $U$, it is affected by the stress tensor $\boldsymbol{\varepsilon}$ and strain tensor $\boldsymbol{\sigma}$, obtained from the FE analysis at that point. This shows how if a bone unit is over stimulated, meaning that it has high mechanical actions for its given density, the remodelling law will tend to increase the bone density at that point to drive it towards the equilibrium or reference stimulus. And vice versa, if bone is understimulated, it will reabsorb.

From the remodelling response rate $\dot{r}$ (Eq. (7)), which is the net tissue volume formed or resorbed per unit time and unit surface available, the actual density variation can be obtained through Eq. (8).

$$\dot{r} = \begin{cases} c_a(\psi_t - \psi_t^* + w) & \text{for } \psi_t \geq \psi_t^* + w \\ 0 & \text{for } \psi_t > \psi_t^* - w \text{ and } \psi_t < \psi_t^* + w \\ c_r(\psi_t - \psi_t^* - w) & \text{for } \psi_t \leq \psi_t^* - w \end{cases} \tag{7}$$

$$\dot{\rho} = kS\hat{\rho}\dot{r} \tag{8}$$

$kS$ being the available specific surface (in mm$^2$/mm$^3$) and obtained using the equation used in [21].

Fig. 4 shows how the density update is integrated into a patient specific remodelling loop. Consider a set of simulation parameters $\mathbf{X}$ and an input 3D medical image $\mathbf{I}_0$. The latter is translated into the numerical computing environment FEAVox, where the technology cgFEM (see Section 2.1) is applied to obtain the strain $\boldsymbol{\varepsilon}_i$ and stress $\boldsymbol{\sigma}_i$ tensors which drive the remodelling process, obtaining the remodelled image $\mathbf{I}_{i+1}$ after one simulation day. The FE analysis is conditioned by the set of finite element simulation parameters $\mathbf{X}^{FE}$ and the set $\mathbf{X}^{Rem}$ which contains the parametrization affecting the remodelling update phase.

As shown in Fig. 4, this process is repeated until convergence, where $c_h$, a metric based on the density variation after each remodelling update, is below a threshold value $c_h^*$.

The computation of $c_h$ is described as:

$$c_h = \frac{\|\mathbf{I}_{i+1} - \mathbf{I}_i\|}{\|\mathbf{I}_i\|} \tag{9}$$

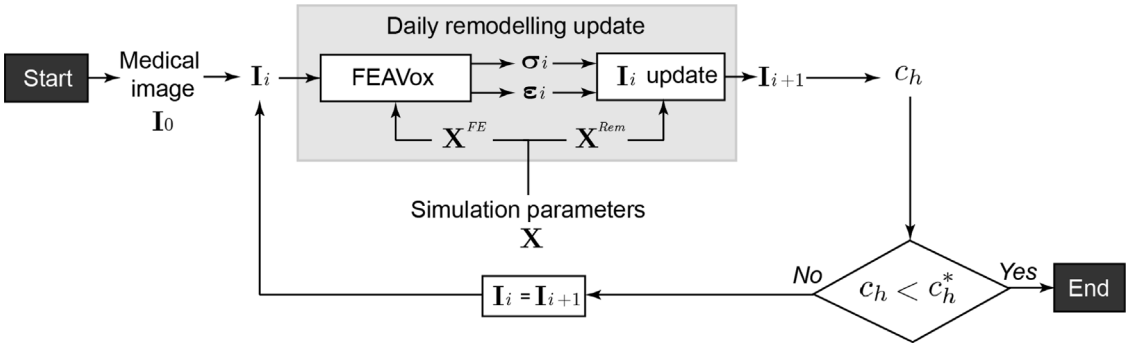


**Fig. 4.** Flow diagram illustrating the remodelling loop.

where the $\|\|$ operator represents the 2-norm, or Frobenius norm of a matrix. For a 3 dimensional $l$-by-$m$-by-$n$ matrix $A$, it is defined as:

$$\|A\| = \sqrt{\sum_{i=1}^{l}\left(\sum_{j=1}^{m}\left(\sum_{k=1}^{n}|A_{ijk}|^2\right)\right)}. \tag{10}$$

Therefore, Eq. (9) is a metric of the relative difference between the input image in iteration $i$, $\mathbf{I}_i$ and the updated image $\mathbf{I}_{i+1}$. Note that the images in this work are numerically expressed as 3 dimensional matrices where the position of each value in the matrix corresponds to the physical voxel locations in the image. It is highlighted that since the 2-norm (which is based in a local, voxel to voxel comparison) is used, spatial variations are taken into consideration.

As shown in Fig. 4, the stopping criterion of a long-term remodelling simulation is defined in the work as the state where $c_h < c_h^*$, representing a sufficiently low density change in relative terms (or homeostatic stability).

### 2.2.1. Smoothing technique

As observed in previous works using the same remodelling model [10] the so called checkerboard effect may occur when applying the remodelling procedure in an element-based approach, presenting undesired density discontinuities. In order to obtain a continuous, physiological bone distribution, a smoothing filtering technique is used to obtain long-term remodelling distributions. More precisely, the filtered density $\rho_{s,v}$ at a given voxel $v$ from the updated one is obtained as a weighted sum function of the density on the surrounding neighbours $\rho_{v,k}...\rho_{v,n_k}$:

$$\rho_{s,v} = \sum_{k=1}^{n_k} \rho_{v,k} w_{s,k} \tag{11}$$

where $w_{s,k}$ is the normalized weight corresponding to neighbour $k$, and depends linear with its distance $d_k$ from the smoothed voxel:

$$w_{s,k} = 1 - \frac{d_k}{r} \tag{12}$$

$r$ being the radius neighbour selection.

## 3. Model parameter fitting

In this section, the parameter identification procedure is explained, first providing a general overview of the data workflow and then explaining the optimization algorithms. Finally, some remarks are given on the effect that different simulation configurations and the solution uniqueness have on the presented technique and the results obtained.

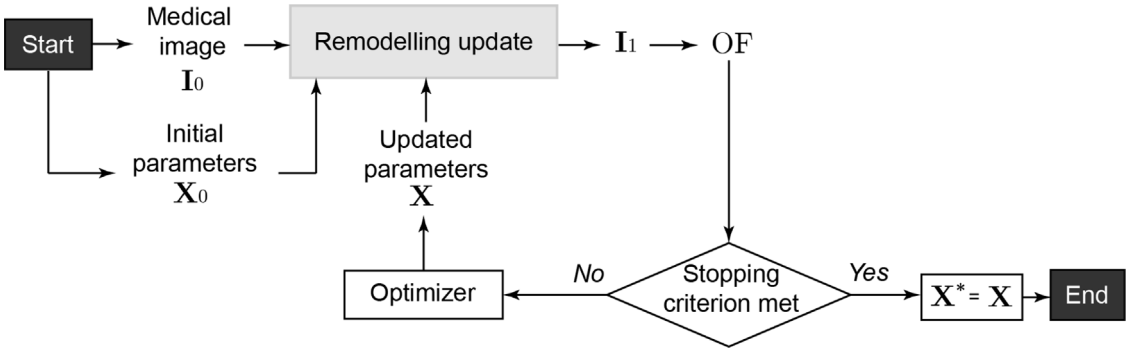


**Fig. 5.** Flow diagram illustrating the parameter fitting procedure. One remodelling step is simulated in order to obtain the density variation between the reference and remodelled images (OF). This difference metric is then used as an error to be minimized through the choice of $\mathbf{X}$, until the convergence of the process, when the optimized parameters $\mathbf{X}^*$ are returned.

### *3.1. Fitting procedure*

Essentially, the objective of this procedure is to estimate a definition of the simulation conditions equivalent to the set of conditions acting on a given patient at the particular moment when the medical image was obtained. The parameter fitting procedure workflow is illustrated in Fig. 5.

We are interested on minimizing an objective function OF, which measures the degree of density variation after one remodelling cycle such as:

$$\mathrm{OF} = \frac{\|\mathbf{I}_1 - \mathbf{I}_0\|}{\|\mathbf{I}_0\| \, n_d}, \tag{13}$$

measuring the relative density difference between image $\mathbf{I}_0$ and the image after 1 remodelling cycle $\mathbf{I}_1$. $n_d$, the number of remodelling days in one full remodelling cycle, is used to average the density variation along the remodelling days, when a different load case is applied each day.

Let us consider that the remodelled image $\mathbf{I}_1$ is obtained given some chosen simulation parameters, $\mathbf{X}$ and initially $\mathbf{X}_0$ (chosen randomly within the search bounds). Assuming that the medical image $\mathbf{I}_0$ was captured at a relatively stabilized (homeostatic) point, an optimal set of simulation parameters $\mathbf{X}^*$ which recreates as much as possible the real scenario, may provide minimum remodelling change OF. Thus, an optimizer is programmed to propose candidate simulation parameters $\mathbf{X}$ until a given stopping criterion based on OF is met. In regard to the optimizer, this work explores two stochastic algorithms, namely Genetic Algorithms and a Bayesian Optimization approach. These are explained in the following section.

It could be argued that in order to ensure that the procedure is searching for a stabilized remodelling scenario, not only in short, but also in the long term, the objective function has to be computed for numerous remodelling cycles. However, the computational cost associated to solving an accurate bone remodelling simulation multiple times for each evaluation of the objective function, makes this approach less practical. Instead, assuming that only one bone density update is representative of the degree of fitness in the choice of $\mathbf{X}$, the methodology proposed can be effective through obtaining OF through 1 remodelling step.

Of course, recreating the actual patient-specific scenario is limited to the defined complexity of the model definition as such, and increasing accuracy would be expected by considering a large extent of biomechanical actions as parameters to be fitted or other patient specific phenomena not integrated in the remodelling model. However, the objective of this work is not to obtain the totality of actual (physical) simulation parameters, but to estimate the combination of only those regarded in the simplified model in order to maximize the stability of bone density variation rate. In other words, even if the set of simulation conditions obtained by the procedure is not the actual physiological one, they are the best possible combination given a simplified, equivalent model.

It is highlighted that the concept of reaching a homeostasis state of the bone is the basis of the parameter adjustment procedure. In fact, the OF value is directly related to bone density variation. Hence, by minimizing OF, the stimulus field is driven to the reference homeostatic point $\Psi_t^*$. This is shown clearly in the results section,

where less apparent density variation is obtained when the loads are applied are those obtained through the proposed procedure.

### 3.2. Parameter optimization strategies applied

Optimization algorithms are widely used to solve iterative parameter searches of complex problems. From the variety of typologies and approaches, this work applies both Genetic Algorithms (GA) [22] and a Bayesian Optimization (BO) [23] strategies.

Genetic algorithms do not require the computation of the derivatives of the objective function with respect to the design variables. Although generally a higher number of evaluations of the objective function is required compared to the BO approach, they tend to global optima even when a relatively large number of design variables are considered [22] or dealing with non convex design spaces. Moreover, GA have been used by the authors when dealing with complex design spaces [24].

Bayesian Optimization is usually preferred when the evaluation of the objective function is computationally expensive [25] (such as in the present work considering the problem size of a medical-image based FEM analysis). As with GA, it is a suitable strategy when there is no access to OF derivatives with the parameters, or when the problem at hand is not known to be convex. Additionally, BO offers an effective combination between exploration of the design space (i.e., avoiding getting trapped in local minima) and its exploitation (approaching the global optimum once the high fitness search area has been detected). This exploration–exploitation blend is driven by the gathered experiments through progressive function evaluations, creating a probabilistic surrogate OF model, normally a Gaussian Process (GP), which contains a predicted mean and variance for all points in the design space. Essentially, the goal is to progressively update the GP function, finally returning the predicted solution, which ideally lies near the real global optimum after meeting some stopping criterion [23].

In the present work, both the GA and BO are applied to the procedure presented in order to study the performance of different optimization algorithms. In the first numerical problem presented: a benchmark problem consisting on a fixed beam, a BO is used. In the medical case study, a GA approach is used.

## 4. Results and discussion

In this section, first the methodology proposed is evaluated through a simple test beam that will be used as benchmark problem, secondly a similar situation to a clinical case study using a real medical image is presented. Although future works will study the identification of parameters affecting the remodelling algorithm $\mathbf{X}^{Rem}$, this work will only focus on the fitting of the set of loads $\mathbf{X}^{FE}$.

### 4.1. Benchmark problem

#### 4.1.1. Obtaining a stabilized image

In order to test the procedure presented in Section 3, a synthetic medical test image is first obtained applying the remodelling loop explained in Fig. 4 from a set of known simulation parameters. These parameters are then searched by the fitting algorithm described in this work. The test image is obtained from the structural problem illustrated in Fig. 6, regarding a beam with a clamped end and a linearly increasing vertical force acting on the top side.

The FE mesh used comprises 53 760 linear cubic elements, with 1 element per voxel (the FE and image mesh being coincident). Starting from an homogeneous material distribution of $\rho_0 = 400$ kg/m$^3$, the bone remodelling process is simulated according to Section 2.2 until a certain degree of homeostatic stabilization is obtained. The magnitude $F_r$ and length $L$ of the linearly distributed force used, as well as the remodelling parameters, are shown in Table 1. Note that $F_r$ is distributed between the equidistantly separed number of node rows $n_{row}$, $L$ being 0.02 m when $n_{row} = 14$. Section 2.2.1 is applied to avoid the checkerboard effect using a filter radius of $r = 2 \cdot \sqrt{3} d_e$ ($d_e$ being the element size). The biological minimum value of the trabecular bone of $\rho_{min} = 100$ kg/m$^3$ and an upper limit of $\rho_{max} = \hat{\rho} = 2100$ kg/m$^3$ are used.

The resultant bone remodelling evolution is represented by the snapshots shown in Fig. 7, while Fig. 8 describes the evolution in global remodelling statistics. As observed, the evolution of the convergence parameter $c_h$ (see

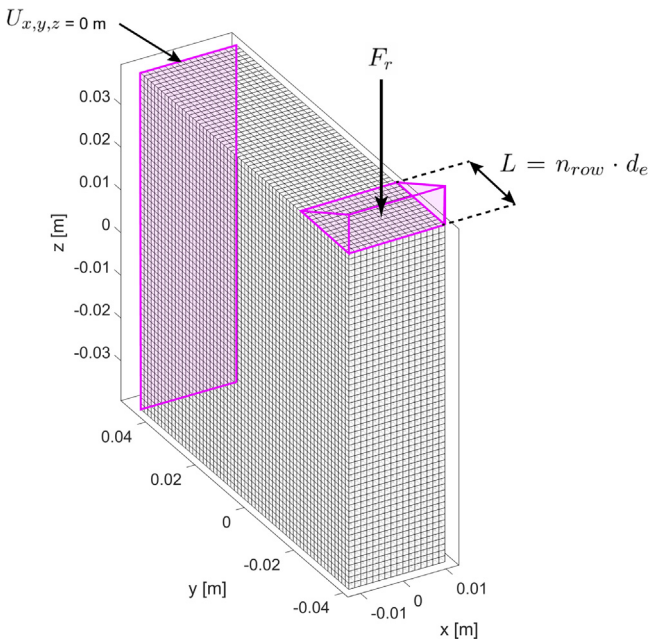


**Fig. 6.** Test beam model showing boundary conditions applied and FE mesh.

**Table 1**
Parameters used in the beam remodelling problem.

| Parameter | $\psi_t^*$ [MPa/day] | $w$ [MPa/day] | $c$ [μm/day] | $n$ [daily cycles] | $F_r$ [N] | $L$ [m] |
|---|---|---|---|---|---|---|
| Value | 50 | 0 | 0.02 | 500 | 800 | 0.02 |

Eq. (9)) is monotonically decreasing over the time, indicating that under stable loads, the bone tends to achieve the homeostatic state.

Since there is no available value of $c_h^*$ representing this point in the benchmark problem, the stopping criterion is set to 1000 days, as in [18]. In the problem at hand, the value of $c_h$ evaluated at 1000 days was $c_h = 6.570 \cdot 10^{-4}$.

### *4.1.2. Parameter fitting*

Assuming that the rest of remodelling parameters are fixed and known, the boundary conditions $F_r$ and $L$ are searched ($\mathbf{X}^{FE} = \{F_r, L\}$) using the procedure explained in Section 3.1 . In this case, the objective function (OF) is computed using image $\mathbf{I_0}$ and $\mathbf{I}_1$ as the image at days 1000 and 1001, respectively. Here, $n_d = 1$ day, since the remodelling step, or cycle is comprised of a single loading case.

As explained in Section 3.2, a Bayesian Optimization (BO) is used for this problem. The density distribution can be considered representative of a given set of $\mathbf{X}$ up to an image stability degree of $c_h^*$. As said, the value of $c_h$ after 1000 days represents the homeostatic state, hence we consider it as $c_h^*$. Therefore, OF $< c_h^*$, when evaluating $\mathbf{X}$, is used as stopping criterion.

Fig. 9 reflects the results of the BO driven fitting of parameters $F_r$ and $L$ simultaneously, being the best point observed of $F_r = 798.41$ N and $L = 0.02$ m ($n_{row} = 14$), in only 16 evaluations of the objective function. The effectiveness of the procedure is suggested, since these values are close to those used to generate the medical image.

## *4.2. Human mandible*

### *4.2.1. Introduction*

The following example is a human maxilla (upper jaw) model, obtained and segmented from a medical $512^3$ voxel sized CT-Scan through the software 3D-Slicer [26], expressed in Hounsfield Units (HU). For the sake

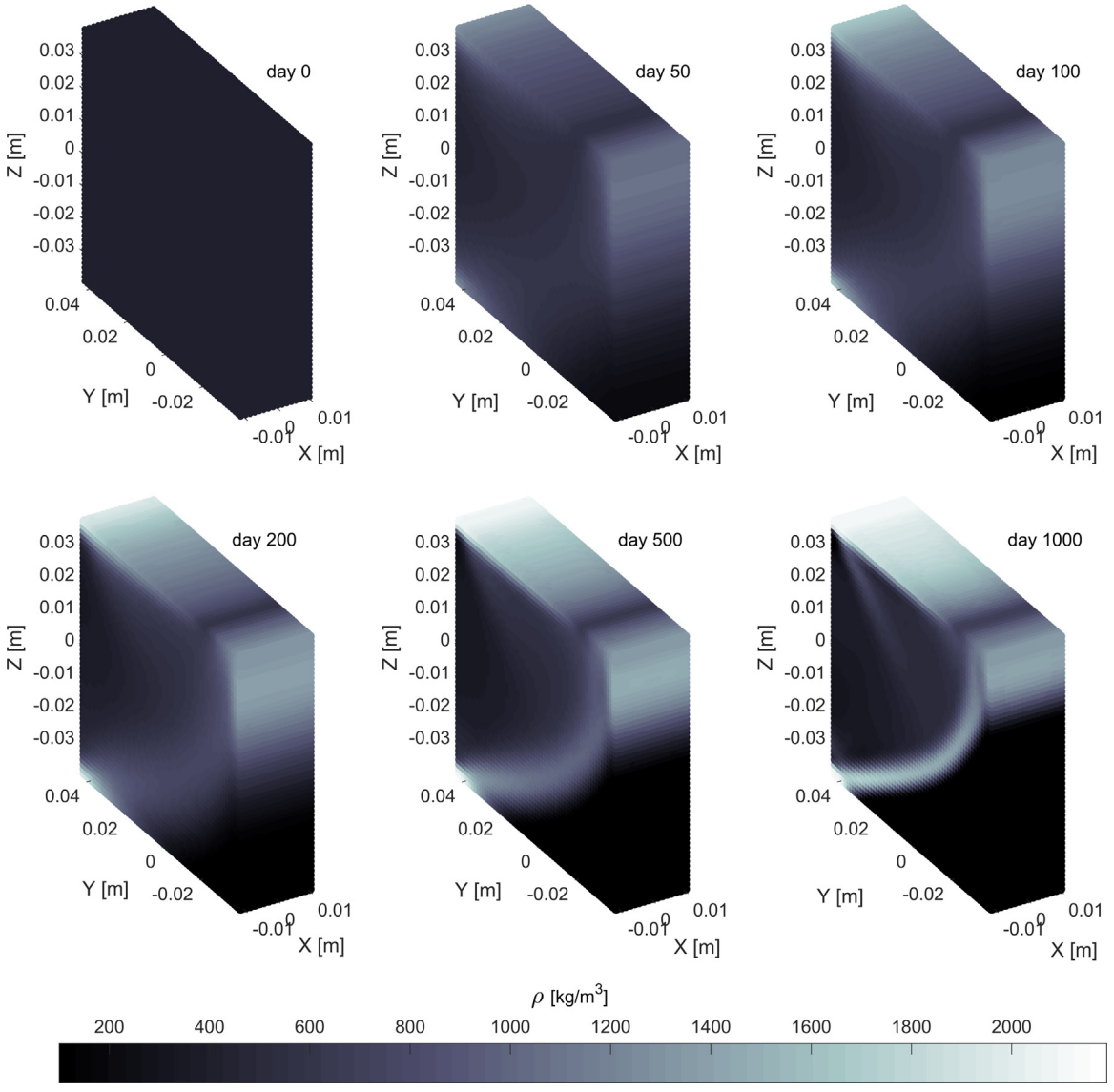


**Fig. 7.** Bone density distribution snapshots at different days of the remodelling process.

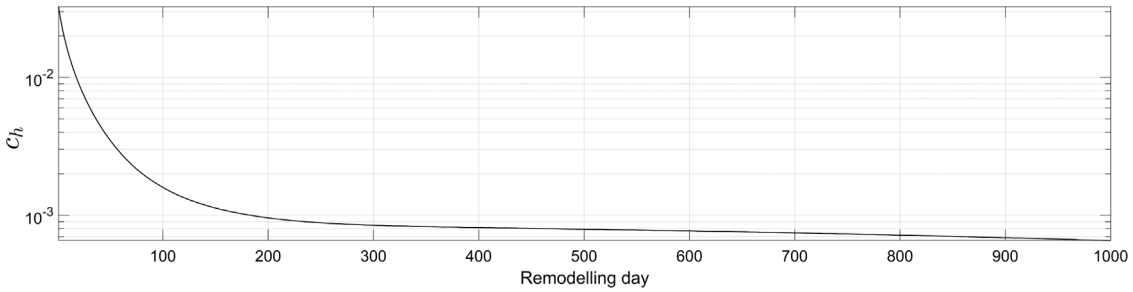


**Fig. 8.** Monotonic evolution of the convergence parameter $c_h$.

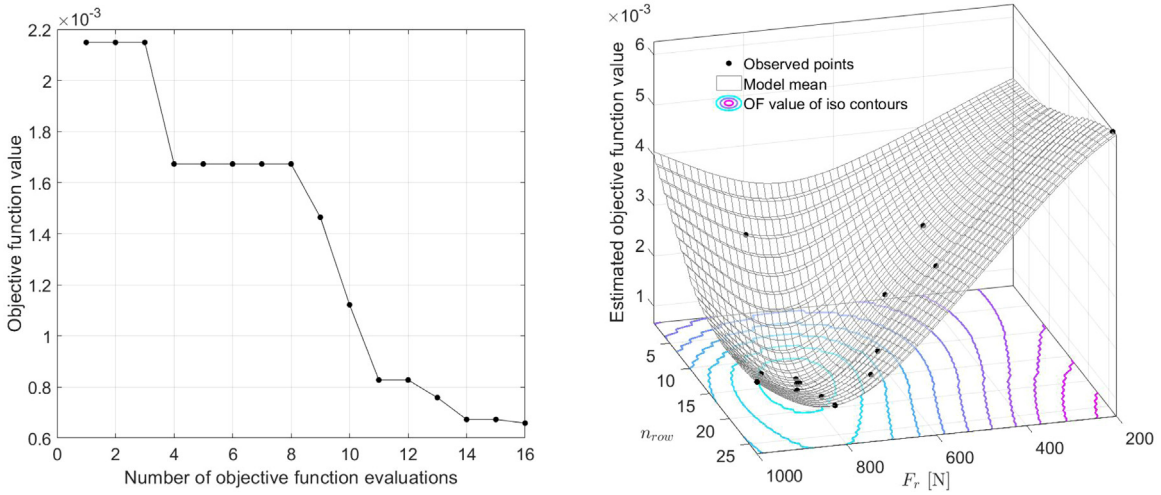


**Fig. 9.** Bayesian optimization statistics. Left: reduction in the objective function value through the BO process. Right: approximated BO model of the response surface.

of computational cost, only half of the complete maxilla is analysed, assuming symmetry conditions. As an approximation, the Hounsfield units to $\rho$ conversion was done through a linear interpolation between the minimum and maximum HU corresponding to bone tissue, and the minimum and maximum bone density values, these being $\rho_{min} = 100$ kg/m$^3$ and $\hat{\rho} = 2100$ kg/m$^3$, respectively. As in the previous example, the smoothing filter explained in Section 2.2.1 is applied to avoid checkerboard effect using a filter radius of $r = 2 \cdot \sqrt{3} d_e$.

Fig. 10 shows a representation of the medical image used, identifying the dental anatomy, where I1 and I2 are the two incisors, C is the canine, P1 (named P from now on) the first premolar and M1 and M2 the first and second molars, respectively.

This particular patient presents a missing teeth (the second premolar). A relevant Region of Interest (ROI), (see Fig. 10) of bone above the teeth can be identified when evaluating the implantation of a potential prosthesis. This region is chosen for practical purposes since is the closer volume to the teeth with easily identifiable bone. Therefore, both the remodelling process and computation of OF to guide the parameter fitting procedure is limited to this region.

Finally, it is commented that the effect of contact pre stresses in the human mandible or body loads are not considered in this preliminary work. Their contribution to the obtained stimuli fields, and thus their potential effect on the outcomes of the procedure could be analysed in the future.

### *4.2.2. Parameter fitting*

A physiological boundary condition configuration is of high importance when aiming to predict short and long term bone distribution. Given the high complexity [9] and patient variability in the loading scenario, such as that exerted in the maxilla during the masticatory cycle, instead of deducing the loads through a biomechanical model [8], this work proposes the implementation and fitting of an equivalent loading scenario in the 4 teeth surrounding the ROI selected (Canine C, Premolar P, Molar1 M1 and Molar 2 M2).

Fig. 11 illustrates the discretization mesh and BCs used. In regard to the Dirichlet boundary conditions, symmetric displacement constraints are applied to the nodes located at three bounding lateral planes, as shown in Fig. 11. The FE mesh remains constant along the remodelling process, and consists of 45 216 linear hexahedral elements of length $d_e = 0.0016$ m, with 51 025 nodes.

One of the model simplifications is to consider direct nodal forces instead of Neumann conditions (surface loads). It can be said that by Saint-Venant principle [27], the numerical singularities created at force application points do not have any relevant effect in the ROI studied. Additionally, since the superior maxilla transmits the loads in the vertical direction, the tooth influence region is close to the tooth. Then the incisors have small influence in the ROI and are not considered in the analysis.

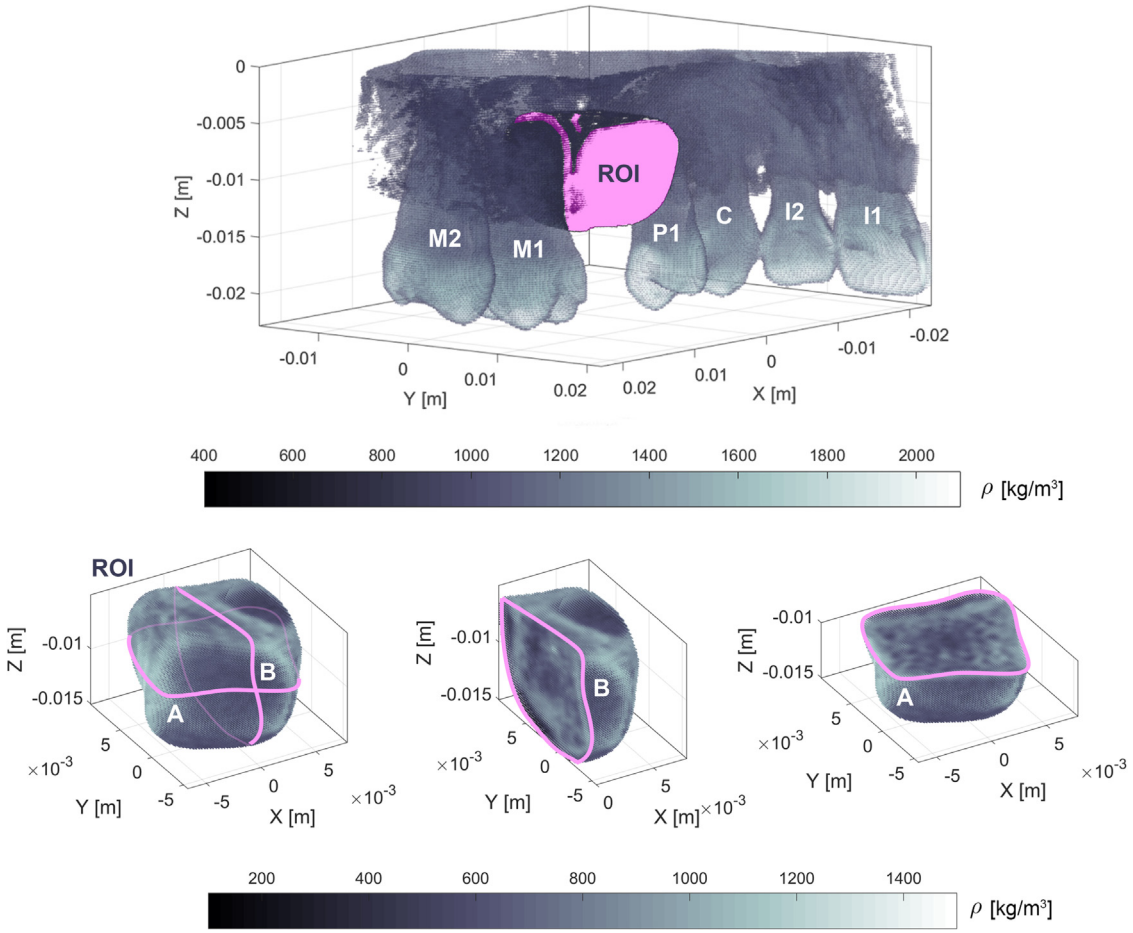


**Fig. 10.** Human bone mandible analysed. Top: views of the medical image with the dental anatomy identified. Bottom: detail views of the Region Of Interest (ROI) selected. Note that voxels with density lower than 400 kg/m$^3$ (in the Top image) and 100 kg/m$^3$ (in the Bottom image) are hidden for representation purposes.

**Table 2**
Masticatory sequence in one considered remodelling cycle.

| Day of cycle | 1 | 2 | 3 | 4 | 5 | 6 | 7 | 8 | 9 | 10 |
|---|---|---|---|---|---|---|---|---|---|---|
| Active tooth | C | P | M1 | M2 | P | M1 | M2 | P | M1 | M2 |

In this case study, a complete remodelling cycle is understood as the one which considers the occlusion forces in all considered teeth following a given masticatory pattern. For this, the sequence applied in [8], is adapted to the teeth which are studied (those near the ROI, in only half of the mandible), and shown in Table 2. In this context, the objective function is computed as in the beam model problem (see Eq. (13)), where $\mathbf{I}_1$ is the ROI image after one remodelling cycle ($n_d = 10$ remodelling days), and $\mathbf{I}_0$ is the original ROI from the medical image.

The multiple load scenario presented is treated as a daily remodelling problem where each tooth is active independently in each day, instead of applying a complex load scenario [28]. This approach is a common simplification and has small influence in the long term remodelling process [8]. We consider a daily number of actions $n = 500$ in each teeth, the reference stimulus is set to $\psi_t^* = 10$ MPa and the growth rate in apposition and resorption is $c_r = c_a = 0.02$ μm/day.

This work studies the relative influence on bone remodelling activity of each of the 4 analysed teeth in order to simplify the complete fitting of loads to those with higher remodelling influence in the ROI selected. As explained

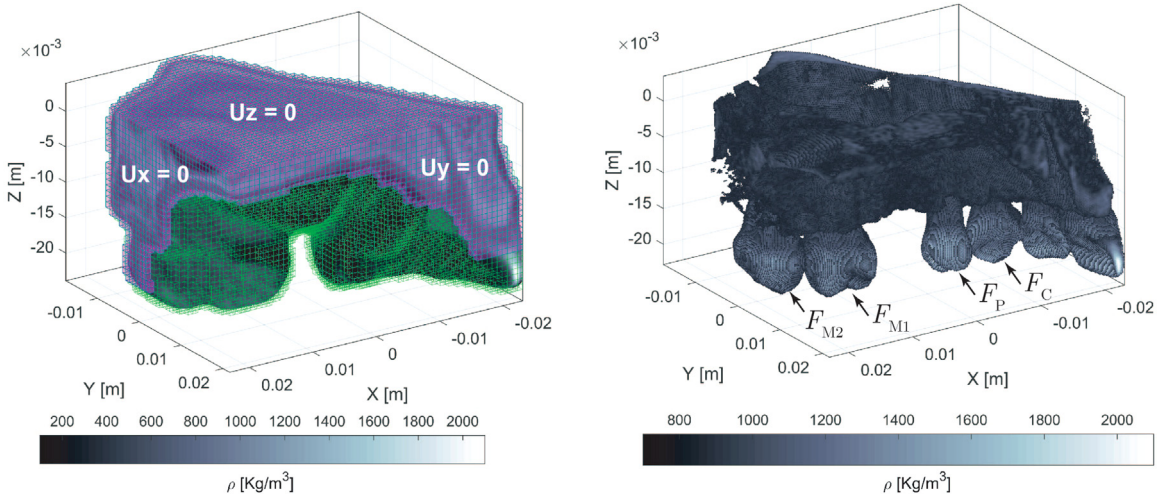


**Fig. 11.** FE model used. Left: Mesh (green) and symmetry boundary conditions applied (purple). Right: point forces applied (voxels under 700 kg/m$^3$ are not shown). (For interpretation of the references to colour in this figure legend, the reader is referred to the web version of this article.)

**Table 3**
Sensitivity analysis results.

| Load case | Compressive tooth load [N] | | | | OF value | Variation [%] |
|---|---|---|---|---|---|---|
| | $F_C^z$ | $F_P^z$ | $F_{M1}^z$ | $F_{M2}^z$ | – | – |
| Reference | 175 | 365 | 365 | 365 | 0.003237 | – |
| I | 175 · 1.1 | 365 | 365 | 365 | 0.003260 | 0.69104 |
| II | 175 | 365 · 1.1 | 365 | 365 | 0.003518 | 8.6767 |
| III | 175 | 365 | 365 · 1.1 | 365 | 0.003392 | 4.7671 |
| IV | 175 | 365 | 365 | 365 · 1.1 | 0.003285 | 1.4884 |

later, instead of fitting the forces of these 4 teeth, a sensitivity analysis is performed to assess the relative importance of each of the loaded teeth in terms of remodelling at the ROI space. This is done by comparing the Objective Function (OF) value obtained after one remodelling cycle applying literature loads taken from [29], with the OF value obtained after one remodelling cycle with applying a small variation (10%) on these reference compressive loads on each of those 4 teeth separately. The results are shown in Table 3. As observed, C and M2 are notably less relevant, and so, the remodelling at the ROI is less sensitive to the loads at those teeth, the effect on the OF being of low significance. The same can be said if we considered the effect of the lateral loads $F_x$ and $F_y$ of each of the dental parts, since they are generally of lower intensity than the occlusal value ($F_z$).

Given the above, we present a protocol, shown in Fig. 12, that provides the equivalent forces through a sequence of steps explained in this Section. This process/protocol finds first the main compressive component in all the four teeth (Step 1), then in Step 2 this compressive load is corrected in the P and M2 teeth. Finally, in Step 3, lateral forces are fitted in the P and M2 teeth.

As explained in Section 3.2, a Genetic Algorithm (GA) is used to search for the optimum force in each Step. The selected GA population size is 10 times the number of variables in each search step (1 variable in Step 1, 2 in Step 2 and 4 variables in Step 3). In all Steps, we considered that GA convergence is met when the variation in the OF value is lower than $0.1 \cdot 10^{-5}$ in the last 50 OF evaluations. For the sake of computational cost, a discretization of the design space of 1 N is used to the define the forces. Finally, in regard to the computational cost, a single evaluation of the OF is completed after a mean of 120.2 s. The simulations were carried out in a PC equipped with a Intel(R) Core(TM) i7-8700 K CPU @ 3.70 GHz and 64 GB of RAM.

**Table 4**
Load configuration for the fitting of the regularized force $F_R^z$ at all 4 preselected teeth. Values in magenta are search parameters, the rest shown are constant.

| Tooth | $F_x$ [N] | $F_y$ [N] | $F_z$ [N] |
|---|---|---|---|
| C | 0 | 0 | $F_R^z \cdot 0.48$ |
| P | 0 | 0 | $F_R^z$ |
| M1 | 0 | 0 | $F_R^z$ |
| M2 | 0 | 0 | $F_R^z$ |

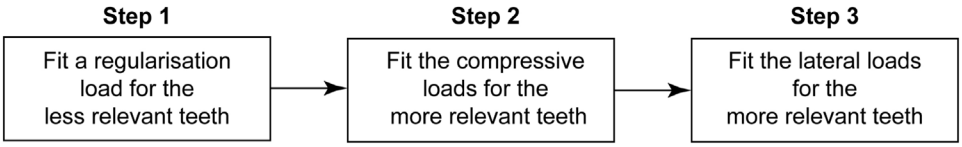


**Fig. 12.** Load fitting protocol followed for the human mandible case study.

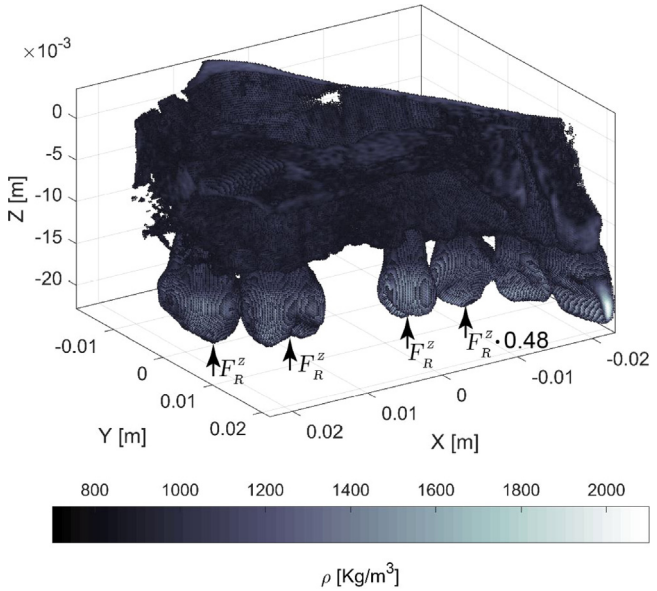


**Fig. 13.** A common regularized force is searched using the fitting procedure with a unique variable.

**Step 1:**

According to [29], the maximum occlusal loads take the following values 13: $F_{M2} = F_{M1} = F_P = F_z$ and $F_C = 0.48 \cdot F_z$, with $F_z = 365$ N. Since it is unreasonable to use $F_z = 365$ N as this is a maximum value, the relationship between loads between the considered teeth from [29] is maintained and a value of $F_z$ that minimizes remodelling is searched ($\mathbf{X}^{FE} = F_z$), this value is selected as regularization value $F_R^z$, and is used in the rest of Steps. The mentioned is performed by running the load fitting procedure with one design variable, supposing a common $F_R^z$ acting on all 4 preselected teeth (see Fig. 13) except at the canine, which is by a factor of 175/365 $\approx$ 0.48, taking in account the relationship between loads at C and P found in literature [29]. This is synthesized in Table 4.

The search evolution for the mentioned regularized force is observed in the data shown in Fig. 14. The search design range is decided to be sufficiently wide ([0,500] N), obtaining a solution of $F_R^z = 111$ N.

**Step 2:**

Using the forces obtained in Step 1 for C and M2, in Step 2 another parameter fitting procedure is then applied to obtain the compressive loads at the P and M1 teeth, as seen in Table 5. Here, $\mathbf{X}^{FE} = \{F_P^z, F_{M1}^z\}$.

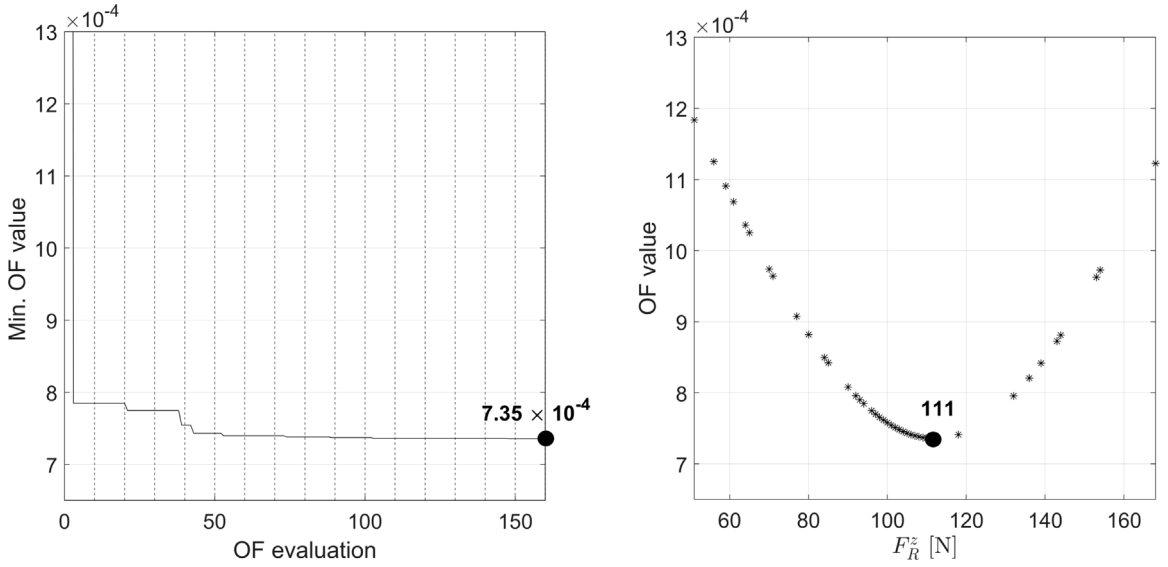


**Fig. 14.** Optimization for the evaluation of teh regularized force $F_R^z$. Left: minimum observed OF values along iterations. Right: OF values of the points observed and solution highlighted.

**Table 5**
Load configuration for the fitting of the compressive loads at P and M1. Values in magenta are search parameters, values in black are constant.

| Tooth | $F_x$ [N] | $F_y$ [N] | $F_z$ [N] |
|---|---|---|---|
| C | 0 | 0 | 111 · 0.48 |
| P | 0 | 0 | $F_P^z$ |
| M1 | 0 | 0 | $F_{M1}^z$ |
| M2 | 0 | 0 | 111 |

**Table 6**
Final load configuration after the fitting of the lateral loads at P and M1. Values in magenta are search parameters, the rest shown are constant.

| Tooth | $F_x$ [N] | $F_y$ [N] | $F_z$ [N] |
|---|---|---|---|
| C | 0 | 0 | 111 · 0.48 |
| P | $F_P^x$ | $F_P^y$ | 89 |
| M1 | $F_{M1}^x$ | $F_{M1}^y$ | 148 |
| M2 | 0 | 0 | 111 |

The GA evolution for this case is represented in Fig. 15, where again a good convergence of the algorithm and a smooth, convex response surface is seen. The solution observed corresponds to the forces $F_P^z = 89$ N and $F_{M1}^z = 148$ N.

**Step 3:**

Finally, in Step 3, the lateral loads of the most relevant teeth ($\mathbf{X}^{FE} = \{F_P^x, F_P^y, F_{M1}^x, F_{M1}^y\}$) are fitted using the information obtained in Steps 1 and 2. The design domain for the X and Y forces in each case are defined as the integer values ranging between lower and upper bounds defined as 50% of each obtained compressive force in Step 2, being [−45,45] N for P and [−74,74] N. When fitting the lateral components of P and M1 using the values previously obtained for the compressive forces (see Table 6), the OF value obtained (see Fig. 16) is improved (decreased) with respect to the purely compressive scenario obtained in Step 2, meaning that a remodelling activity closer to the homeostatic state is obtained.

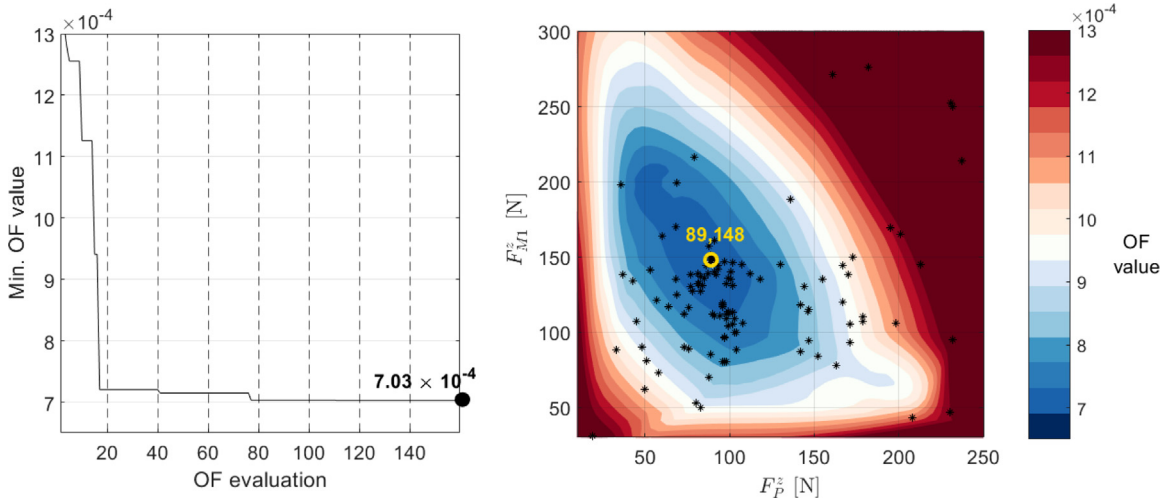


**Fig. 15.** Optimization data for the fitting of the vertical occlusal forces $F_P^z$ and $F_{M1}^z$. Left: minimum observed OF values along iterations. Right: Response surface obtained interpolating with the points observed and solution highlighted.

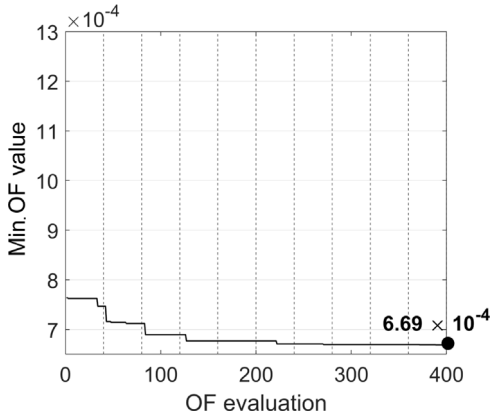


**Fig. 16.** Optimization data for the fitting of $F_P^x$, $F_P^y$, $F_{M1}^x$, $F_{M2}^y$ describing the minimum observed OF values along OF evaluations.

**Table 7**
Load configuration for the fitting of the lateral loads at P and M1.

| Tooth | $F_x$ [N] | $F_y$ [N] | $F_z$ [N] |
|---|---|---|---|
| C | 0 | 0 | $111 \cdot 0.48$ |
| P | −26 | 16 | 89 |
| M1 | 22 | −56 | 148 |
| M2 | 0 | 0 | 111 |

### *4.2.3. Discussion*

The solution obtained (shown in Table 7) is within the order of magnitude of the values used in [30], which evaluated the long term remodelling of dental pieces, in the compressive force magnitude and the compressive–lateral component relationship.

In literature it is difficult to find reference values of dental occlusion forces for the simulation of a typical masticatory cycle (dynamic bite force) [31]. This is due to the fact that it is difficult to measure real-life masticatory activity, being most of the studies focused on maximum bite forces [32,33], or the relationship between force directions given compressive force [34].

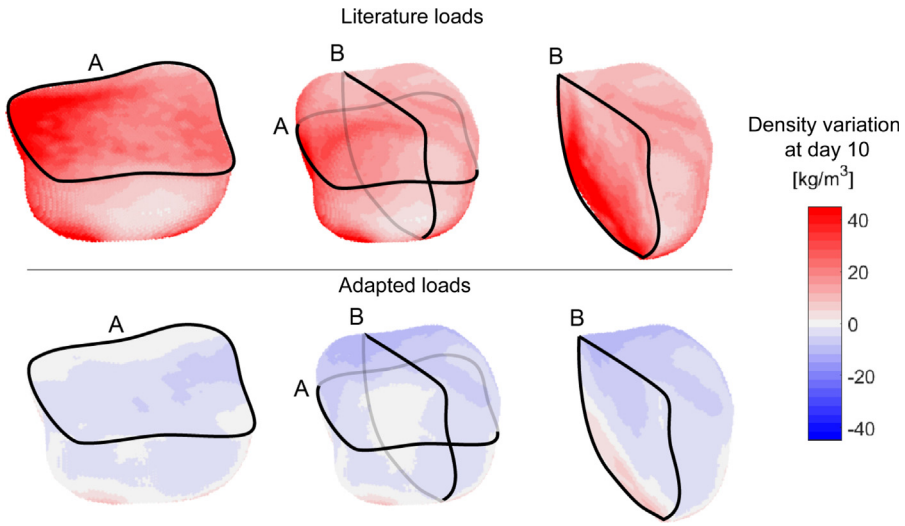


**Fig. 17.** Bone density variation at the ROI after one 10 day remodelling cycle using literature maximum values (Top) and the adapted loads obtained (Bottom).

Figs. 17 and 18 show the bone density variation at the ROI after a 10-day remodelling cycle (Fig. 17) and 50 days (Fig. 18). The figures show this variation for 2 load case scenarios: (a) Maximum bite forces on teeth obtained from literature [29], and (b) masticatory forces evaluated with the methodology proposed in this paper (values shown in Table 7). As seen in the figures, if the maximum bite forces obtained from literature were used as simulation input, the remodelling distribution obtained both in the short and long terms will differ from the physiological scenario obtained. In fact, after a 10-day remodelling cycle the OF value considering maximum masticatory forces is relatively high ($3.24 \cdot 10^{-3}$) when compared to the OF value for the BFS shown in Table 7 ($6.69 \cdot^{-4}$). In the long term (see Fig. 18 for the evolution of remodelling in a 50-day period), the literature load scenario creates a highly deviatory trend with respect to the original medical image, while the adapted load scenario maintains a bone density distribution very similar to the original image. This information is also illustrated in Fig. 19 that shows the difference with respect to the reference medical image applying each load scenario.

As seen, as additional parameters are adopted as inputs through the workflow proposed, increasingly homeostatic scenario is obtained. When studying the complexity of the optimization problem as such, it is interesting to appreciate that starting from the OF value when the literature loads are considered, the enriching process followed by Steps 1–3 produces a considerable reduction in the OF, but of course it comes with a larger computational cost as measured on OF evaluations, as seen in Fig. 20. The user can finally make a trade off to select the better option according to the needs.

## 5. Conclusions

Accurate short and long term bone remodelling simulation is crucial for in the realm of patient-specific medical applications, such as prosthesis or rehabilitation design. An *in-silico* approach is largely affected by uncertainties in biomechanical parameters, thus, the present methodology is presented as an efficient tool to reduce these uncertainties by the fitting of these parameters using the stabilized medical image.

Assuming certain homeostatic equilibrium in the medical image, the procedure is able to identify boundary conditions which are close or equivalent to the physiological ones. This is particularly relevant, since such boundary conditions are very difficult to measure, specially in a clinical set-up. In contrast, the methodology presented only requires as patient specific data a medical image, typically obtained previous to interventions. Importantly for its potential application in a medical protocol, the optimization procedure presented is computationally efficient only the optimization algorithm to consider requiring the simulation of one remodelling cycle for the evaluation of the objective function.

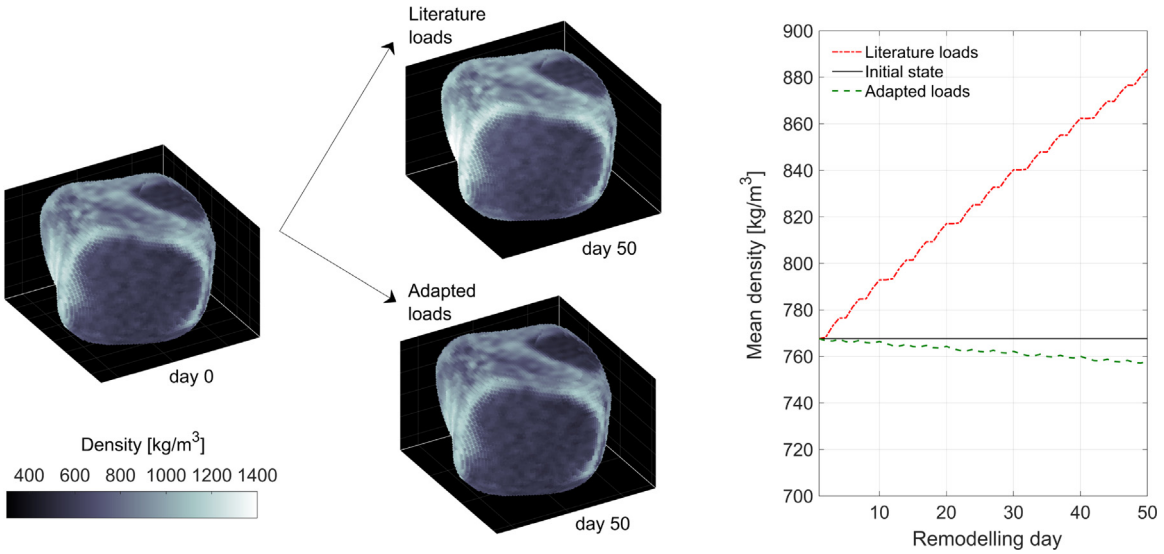


**Fig. 18.** Long term remodelling data at the ROI with different load scenarios. Left: image data at days 0 and 50. Right: mean density evolution.

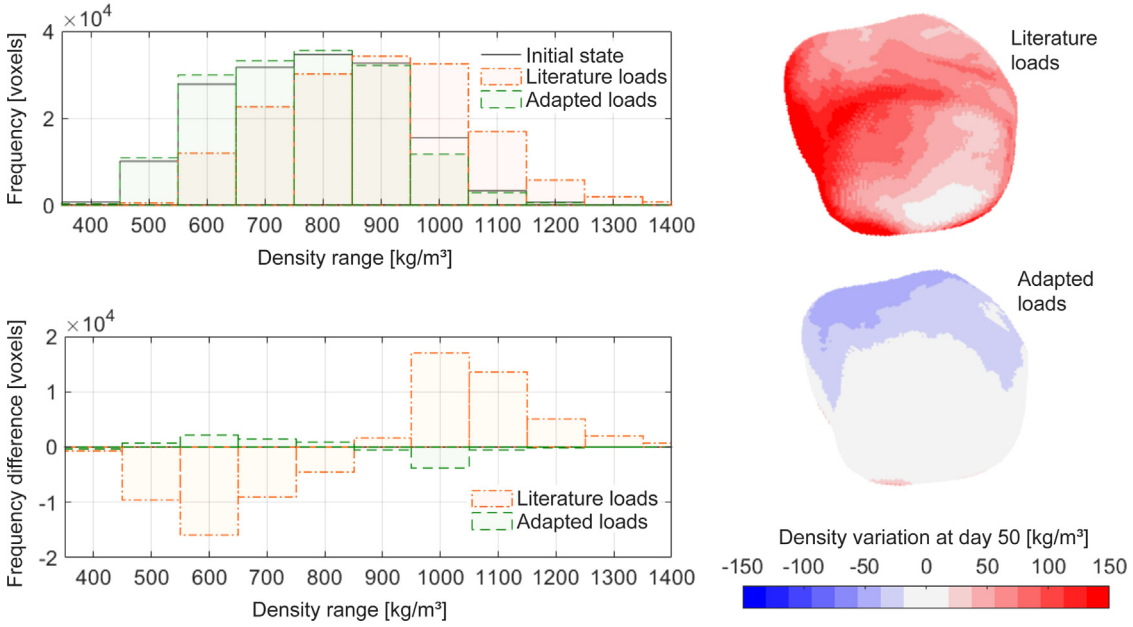


**Fig. 19.** Difference at remodelling day 50 with respect to the initial medical image using the literature and adapted loads. Left Top: image histogram comparison, where negative/positive frequency differences indicate reduction/increase in a particular density range. Left Bottom: difference in voxels of each of the ranges shown. Right: image showing the density variation.

The results obtained in a synthetic beam example, where the procedure is effectively able to find the load amplitude and location applied for the generation of a specific long-term bone distribution, suggest a good numerical performance of the procedure. When applying the methodology to a real human mandible problem, the fitting of applied force vectors result in simulation conditions which minimize bone remodelling, and as expected, when considering additional parameters, i.e. load directions of the simulation model, leads to lower values of the OF.

In order to further explore the capabilities of the proposed methodology, more experimentation is still required using more complex load scenarios and additional simulation parameters. This can be done by including also those

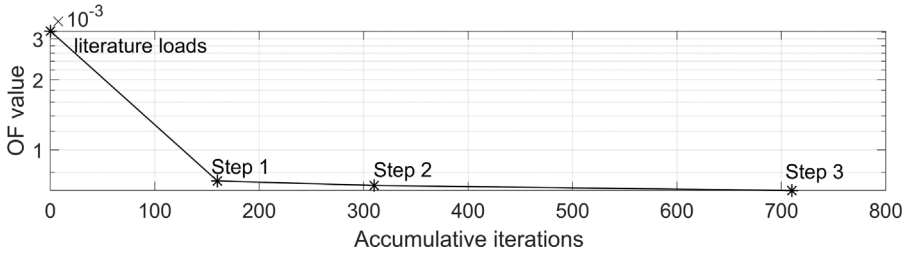


**Fig. 20.** OF Value relationship with the computational cost, measured as the accumulated OF evaluations after each of the Steps explained.

specific biomechanical variables in the remodelling algorithm which are very difficult to measure but are related with the bone distribution observed in the medical image, such as the reference stimulus $\psi_i^*$. Additionally, parameters, such as $c_r$ ir $c_a$, which affect the dynamic evolution of the remodelling process can potentially be identified if the OF is computed using various medical images in different instants of the bone remodelling process. Other extensions to improve the accuracy of the method could include applying $h$-adaptative mesh refinement based on the image heterogeneity [14] or using goal-oriented approaches [35,36]. Future works could also include techniques to identify model parameters given some measurable patient specific data, which could improve the efficiency and outcomes of fitting process. As an example, the Bayesian approach for accounting for model uncertainties in [37] could be used. Finally, other recently developed tools in the field of machine learning [38] could enrich the fitting procedure if suitable training data was available.

## Declaration of competing interest

The authors declare no conflict of interest.

## Data availability

Data will be made available on request.

## Acknowledgements

The authors gratefully acknowledge the financial support of Generalitat Valenciana (FEDEGENT/2018/025 and Prometeo/2021/046), Ministerio de Economía, Industria $y$ Competitividad (DPI2017-89816-R) and FEDER. Funding for open access charge: CRUE-Universitat Politècnica de València.

## References

[1] J. Wolff, The Law of Bone Remodelling, Springer Berlin Heidelberg, 1986.
[2] A.G. Robling, C.H. Turner, Mechanical signaling for bone modeling and remodeling, Crit. Rev. Eukaryot Gener. Expr. 19 (2009) 319–338.
[3] R. Huiskes, H. Weinans, B. van Rietbergen, Stress shielding and bone resorption, Clin. Orthop. Relat. Res. 274 (1991) 124–131.
[4] N. Tan, R.J. van Arkel, Topology optimisation for compliant hip implant design and reduced strain shielding, Materials 14 (2021) 7184.
[5] P. Christen, K. Ito, R. Ellouz, S. Boutroy, E. Sornay-Rendu, R.D. Chapurlat, B. van Rietbergen, Bone remodelling in humans is load-driven but not lazy, Nature Commun. 5 (2014) 4855.
[6] M. Doblaré, J.M. García, Anisotropic bone remodelling model based on a continuum damage-repair theory, J. Biomech. 35 (2002) 1–17.
[7] D. Santonocito, F. Nicita, G. Risitano, A parametric study on a dental implant geometry influence on bone remodelling through a numerical algorithm, Prosthesis 3 (2021) 157–172.
[8] J.M. Reina, J.M. García-Aznar, J. Dominguez, M. Doblaré, Numerical estimation of bone density and elastic constants distribution in a human mandible, J. Biomech. 40 (2007) 828–836.
[9] M.S. Commisso, J.M. Reina, J. Ojeda, J. Mayo, Finite element analysis of the human mastication cycle, J. Mech. Behav. Biomed. Mater. 41 (2015) 23–35.
[10] J.M. Reina, J. Ojeda, J. Mayo, On the use of bone remodelling models to estimate the density distribution of bones. Uniqueness of the solution, PLoS One 1 (2015) 11–12.

[11] P. Christen, B. van Rietbergen, F.M. Lambers, R. Müller, K. Ito, Bone morphology allows estimation of loading history in a murine model of bone adaptation, Biomech. Model Mechanobiol. 11 (2012) 483–492.
[12] P. Christen, K. Ito, I. Knipples, R. Müller, G.H. van Lenthe, B. van Rietbergen, Subject-specific bone loading estimation in the human distal radius, J. Biomech. 46 (2013) 750–766.
[13] J.M. Reina, J. Ojeda, J. Mayo, On the use of bone remodelling models to estimate the density distribution of bones. Uniqueness of the solution, PLoS One 1 (2015) 11–12.
[14] L. Giovannelli, J.J. Rodenas, J.M. Navarro-Jimenez, M. Tur, Direct medical image-based finite element modelling for patient-specific simulation of future implants, Finite Elem. Anal. Des. 136 (2017) 37–57.
[15] M. Tur, J. Albelda, O. Marco, J.J. Rodenas, Stabilized method of imposing Dirichlet boundary conditions using a recovered stress field, Comput. Methods Appl. Mech. Engrg. 296 (2015) 352–375.
[16] J.M. Navarro-Jiménez, E. Nadal, M. Tur, J. Martínez-Casas, J.J. Rodenas, On the use of stabilization techniques in the cartesian grid finite element method framework for iterative solvers, Internat. J. Numer. Methods Engrg. 121 (2020) 3004–3020.
[17] G.S. Beaupré, T.E. Orr, D.R. Carter, An approach for time-dependent bone modeling and remodeling-application: a preliminary remodeling simulation, J. Orthop. Res. 5 (1990) 663–670.
[18] M. Mengoni, J.P. Ponthot, An enhanced version of a bone-remodelling model based on the continuum damage mechanics theory, Comput. Methods Biomech. Biomed. Eng. 18 (2014) 1367–1376.
[19] F.J. Reina, J. Ojeda Granja, J.M. Mayo Núñez, On the use of bone remodelling models to estimate the density distribution of bones. Uniqueness of the solution, PLoS One 11 (2016) 828–836.
[20] C.J. Hernandez, G.S. Beaupré, T.S. Keller, D.R. Carter, The influence of bone volume fraction and ash fraction on bonestrength and modulus, Bone 29–1 (2001) 74–78.
[21] P. Pivonka, P.R. Buenzil, S. Sheiner, C. Helmich, C.R. Dunstain, The influence of bone surface availability in bone remodelling — A mathematical model including coupled geometrical and biomechanical regulations of bone cells, Eng. Struct. 47 (2013) 134–143.
[22] D.E. Goldberg, Genetic Algorithms in Search, Optimization, and Machine Learning, thirteenth ed., Addison Wesley, 1989.
[23] F. Archetti, A. Candelieri, Bayesian Optimization and Data Science, in: Springer Briefs in Optimization, Springer, Cham, 2019.
[24] J. Gutiérrez-Gil, X. García-Andrés, J. Martínez-Casas, E. Nadal, F.D. Denia, Optimized perforation schemes in railway wheels toward acoustic radiation mitigation, J. Vib. Acoust. 142 (2020) 041009.
[25] S. Gregori, J. Gil, M. Tur, J.E. Tarancón, F.J. Fuenmayor, Analysis of the overlap section in a high-speed railway catenary by means of numerical simulations, Eng. Struct. 221 (2020).
[26] R. Kikinis, S.D. Pieper, K. Vosburgh, 3D Slicer: A Platform for Subject-Specific Image Analysis, Visualization, and Clinical Support. Intraoperative Imaging Image-Guided Therapy, A. F.Editor, ISBN: 978-1-4614-7656-6, 2014, pp. 277–289, 3(19)-3.
[27] A.J.C.B. Saint-Venant, Memoire sur la torsion des prismes, Mem. Divers Savants 14 (1855) 233–560.
[28] C.R. Jacobs, Numerical Simulation of Bone Adaptation to Mechanical Loading (Ph.D. thesis), Stanford University.
[29] E. Helkimo, G.E. Carlsonn, M. Helkimo, Bite force and state of dentition, 35, (1977) 297–303.
[30] K. Su, L. Yuan, J. Yang, J. Du, Numerical simulation of mandible bone remodeling under tooth loading: A parametric study, Nature Sci. Rep. 9 (2019) 14887.
[31] A. Shimada, Y. Yamabe, T. Torisu, L. Baad-Hansen, H. Murata, P. Svensson, Measurement of dynamic bite force during mastication, J. Oral Rehabil. 39 (2012) 349–356.
[32] T.M.G.J. van Eijden, J.H. Koolstra, P. Brugman, W.A. Wejis, A feedback method to determine the three-dimensional bite-force capabilities of the human masticatory system, J. Dent. Res. 67 (1988) 450.
[33] M. Bakke, Bite force and occlusion, Semin. Orthod. 12 (2) (2006) 120–126.
[34] T.E. Southard, R.G. Behrents, E.A. Tolley, The anterior component of occlusal force. Part 1. Measurement and distribution, Am. J. Orthnd. Dmiojac. Orthnp. 96 (6) (1989) 493–500.
[35] H.P. Bui, H. Courtecuisse, M. Audette, S. Cotin, S.P.A. Bordas, S. Tomar, Numerical simulation of mandible bone remodeling under tooth loading: A parametric study, Int. J. Numer. Methods Biomed. Eng. 34 (2017) 5.
[36] M. Duprez, S.P.A. Bordas, M. Bucki, H.P. Bui, F. Chouly, V. LLeras, C. Lobos, A. Lozinski, P. Rohan, S. Tomar, Quantifying discretization errors for soft tissue simulation in computer assisted surgery: A preliminary study, Appl. Math. Model. 77 (2020) 709–723.
[37] H. Rappel, L.A.A. Beex, L. Noels, S.P.A. Bordas, Identifying elastoplastic parameters with Bayes' theorem considering double error sources and model uncertainty, Probab. Eng. Mech. 55 (2019) 28–41.
[38] V. Krokos, V.B. Xuan, S.P.A. Bordas, P. Young, P, Kerfriden a Bayesian multiscale CNN framework to predict local stress fields in structures with microscale features error sources and model uncertainty, Comput. Mech. 69 (2022) 733–766.